# Structural Insights into Ni–Fe Layered Double Hydroxides as Anode Catalysts for Pairing CO2 Reduction and Ethylene Glycol Oxidation

Jiefeng Liu, Yuwei Yang, Eddy Petit, Valérie Bonniol, Zakaria Anfar, Bertrand Rebiere, Bonito Aristide Karamoko, Wensen Wang, Huali Wu, Mathilde Moderne, et al.

# Structural Insights into Ni−Fe Layered Double Hydroxides as Anode Catalysts for Pairing $CO_2$ Reduction and Ethylene Glycol Oxidation

Jiefeng Liu, Yuwei Yang, Eddy Petit, Valérie Bonniol, Zakaria Anfar, Bertrand Rebiere, Bonito Aristide Karamoko, Wensen Wang, Huali Wu, Mathilde Moderne, Robin Guéret, Philippe Miele, Nicholas M. Bedford, Chrystelle Salameh, and Damien Voiry*

ABSTRACT: Harnessing renewable electricity for $CO_2$ electroreduction is essential for the low-carbon production of chemicals and fuels. Traditional methods combine the $CO_2$ reduction reaction ($CO_2RR$) with the oxygen evolution reaction (OER), which has high energy consumption and low-value products. Here, we propose using anodic ethylene glycol oxidation reaction (EGOR) instead of OER, which has a lower oxidation potential and valuable product. Nickel−iron layered double hydroxide (NiFe-LDH) is identified as an efficient EGOR catalyst. Using systematic electrochemical measurements and both ex situ and operando spectroscopy revealed that NiFe-LDH undergoes distinct structural evolution under EGOR and the OER. We found that metal−oxygen hybridization enhances EGOR selectivity and reduces the OER selectivity. Pairing EGOR with $CO_2RR$ allowed achieving a low electrical consumption of 6.2 kWh $Nm^{-3}$ at 300 mA $cm^{-2}$ for CO production using Ag as the cathode. This strategy was successfully applied to the conversion of $CO_2$ to multicarbon products, demonstrating a partial current density of 364 mA $cm^{-2}$ for $C_{2+}$ production using $Cu_2O$ as the cathode.

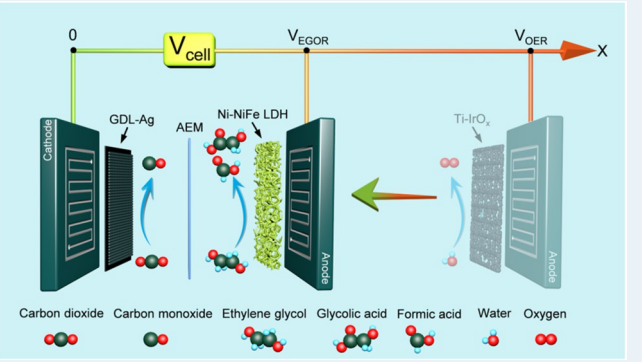


KEYWORDS: *$CO_2$ reduction reaction, NiFe LDH catalyst, ethylene glycol oxidation reaction, electric power consumption, technoeconomic*



## 1. INTRODUCTION

The development of carbon capture, utilization, and storage (CCUS) technology plays a pivotal role in addressing the conversion of emitted carbon dioxide ($CO_2$) and closing the carbon cycle.[1−4] Presently, extensive research is being conducted on the direct electrochemical reduction of $CO_2$ to valuable chemicals and intermediates, including carbon monoxide (CO), formate ($HCOO^-$), methane ($CH_4$), ethylene ($C_2H_4$), and alcohols. These efforts have primarily focused on refining catalysts, optimizing electrolytes, and designing more efficient electrolyzers.[5−7] Additionally, analyzing the technoeconomic feasibility of the entire system is an indispensable part of the process. Verma et al. have recently employed a gross-margin model and the U.S. Department of Energy H2A model to evaluate the technoeconomic viability of $CO_2$ electroreduction. Their findings emphasize the significance of reducing the cell potential as a means to enhance economic feasibility.[8] Currently, in most traditional $CO_2$ electroreduction methods, the cathodic $CO_2$ reduction reaction ($CO_2RR$) is typically coupled with the anodic oxygen evolution reaction (OER). The Gibbs free energy of the OER combined with the sluggish kinetics is responsible for approximately 90% of the total energy consumed by the cell.[8] Additionally, the low value of the generated oxygen (~$25 per ton) has a negligible impact on the economic feasibility of the process.

The utilization of the organic oxidation reaction (OOR) as the anodic reaction has been proposed to address the challenges associated with the high thermodynamic and kinetic requirements as well as the low technoeconomic value of the oxygen evolution reaction (OER). The anodic OOR can generate value-added products to enhance the overall technoeconomic viability of $CO_2$ electroreduction. The combination of cathodic $CO_2RR$ and anodic OOR has been successfully demonstrated in various electrolyzers such as H-cells,[9] flow cells,[8] and membrane electrode assembly (MEA) electrolyzers.[10] Limited attention has, however, been given to understanding the internal mechanism of the OOR in terms of the local atomic structure of the catalyst and achieving a lower

electric power consumption (EPC) at high current densities for practical technoeconomic analysis.

Ethylene glycol (EG) is prominent waste from the automotive and textile industry.[11] Due to its high boiling point, ethylene glycol exhibits reduced volatility when compared to typical alcohols, such as methanol and ethanol. This characteristic makes ethylene glycol a more stable and less volatile option for various applications. One million tons of EG is used as antifreeze each year. While some of this is recycled, a significant portion ends up as waste. The electrochemical oxidation of EG can produce various valuable products, such as glycolaldehyde, glyoxal, glycolic acid, glyoxylic acid, and oxalic acid. These products have versatile applications in industries such as textiles, pharmaceuticals, and cosmetics.[11] While electrooxidation of EG has received relatively less attention compared to the oxidation of compounds like glycerol, glucose, or HDMS, it is important to highlight that glycolic acid holds a market price of about $4000 per ton,[12] which is more than 4 times that of ethylene glycol priced at around $900 per ton.[13] This stark price difference underscores the substantial economic potential of the electrooxidation of ethylene glycol, while offering perspective for EG recycling.[13]

In this study, we propose an alternative approach that combines the $CO_2$RR and ethylene glycol oxidation reactions (EGOR) to replace the traditional OER. By employing a noble-metal-free catalyst, specifically nickel−iron layered double hydroxide (NiFe LDH), as the anode catalyst, we achieved successful conversion of EG. X-ray absorption spectroscopy (XAS) and operando Raman spectroscopy investigations confirmed the structural stability of the as-prepared NiFe LDH under EGOR conditions. Our results reveal the emergence of selective active sites through metal−oxygen hybridization during the anodic process, while the OER induces irreversible structural evolution, where $Ni(OH)_2$ transformed into NiOOH, leading to the formation of NiOOH-NiFe LDH heterostructures. We also found that EGOR conditions minimizing structural defects associated with OER activity. When integrating the $CO_2$RR and the EGOR within an MEA electrolyzer using Ag nanoparticles (Ag-NPs) as the cathode catalyst, a remarkably low full-cell voltage of 1.9 V was attained at a current density of 50 mA $cm^{-2}$, alongside near unity Faraday efficiency (FE) for CO. After further optimizing the reaction conditions, we successfully reduced the cell voltage requirement by 1.3 ± 0.1 V, equivalent to a 38 ± 2% reduction in electricity consumption using Ag-NPs as the cathode catalyst, and by 1.04 V, equivalent to a 31% reduction using $Cu_2O$ as the cathode catalyst. With Ag-NPs as the cathode catalyst, this translates to an impressively low electrical power consumption of merely 6.2 kWh $Nm^{-3}$ at the current density of 300 mA $cm^{-2}$, outperforming the previous results from the literature for MEA electrolyzers. Simultaneously, we achieved a current density of 364 mA $cm^{-2}$ for producing $C_{2+}$ with an FE of ~61% in a two-component electrolyzer using $Cu_2O$ as cathode catalyst. Technoeconomic analysis of energy consumption and the generation at the cathode and anode suggests that profitability could be obtained at current densities exceeding 100 mA $cm^{-2}$.

## 2. MATERIALS AND METHODS

**2.1. Chemicals.** Nickel nitrate hexahydrate [$Ni(NO_3)_2 \cdot 6H_2O$, ≥98.5%], iron(III) nitrate nonahydrate [$Fe(NO_3)_3 \cdot 9H_2O$, ≥98%], silver nanopowder (Ag, <100 nm), iridium(III) chloride hydrate ($IrCl_3 \cdot xH_2O$, ≥99.9%), ethylene glycol ($C_2H_6O_2$, ≥99%), cesium hydroxide monohydrate ($CsOH \cdot H_2O$, ≥99.5%), potassium bicarbonate ($KHCO_3$, ≥99.7%), Nafion perfluorinated resin solution (contains 45% water), and hydrochloric acid (HCl, 37%) were purchased from Sigma-Aldrich. All of the chemicals in the experiment were used without further purification. Carbon black (Ketjenblack EC-600JD), anion exchange membrane (Sustainion X37-50 grade RT), alkaline ionomer (Sustainion XC-2), gas diffusion layer (GDL, Sigracet 22 BB), and titanium mesh were purchased from Fuel Cell Store. All aqueous solutions were prepared using 18.2 MΩ $cm^{-1}$ deionized water.

**2.2. Catalyst Synthesis and Working Electrode Preparation.** *2.2.1. Synthesis of NiFe LDH Electrode.* NiFe LDH was electrodeposited onto the Ni foam. Before the deposition, the Ni foam was sonicated with ethanol, 3 M hydrochloric acid, and deionized water for 30 min, respectively. A 5 mM aqueous electrolyte solution containing $Ni(NO_3)_2 \cdot 6H_2O$ and $Fe(NO_3)_3 \cdot 9H_2O$ in a 1:1 molar ratio was used in the deposition. The deposition was accomplished by applying a constant potential of −1 V with a total charge of 5C to ensure a consistent deposition yield each time.

*2.2.2. Synthesis of Ag Electrode and Ag/CB Electrode.* A mixture of 100 mg of Ag powder (90 mg of Ag and 10 mg of CB for Ag/CB electrode), 15% (w/w) Nafion, and 15% (w/w) XC-2 ionomer was prepared in 2 mL of water and 2 mL of 2-propanol and sonicated for 30 min before spraying. The as-prepared ink was uniformly sprayed onto the gas diffusion layer (GDL) with a loading amount of 1 mg $cm^{-1}$.

*2.2.3. Synthesis of $Cu_2O$ Electrode.* For the synthesis of $Cu_2O$, 241.6 mg of $Cu(NO_3)_2 \cdot 3H_2O$ was dissolved in 30 mL of $H_2O$ in a beaker. Then, 10 mL of 2 M NaOH was added dropwise to the mixture and stirred for 30 min to form $Cu(OH)_2$. Subsequently, 1 g of L-ascorbic acid dissolved in 10 mL of $H_2O$ was added to the mixture while it was heated to 50 °C under stirring. After a 4 h reaction, brick-red precipitates were obtained and washed several times with water and ethanol using centrifugation. Finally, the obtained powder was dried overnight under vacuum. For making the $Cu_2O$ cathode, a mixture of 100 mg of $Cu_2O$ powder, 15% (w/w) Nafion, and 15% (w/w) XC-2 ionomer was prepared in 2 mL of water and 2 mL of isopropanol and sonicated for 30 min before spraying. The as-prepared ink was uniformly sprayed onto the gas diffusion layer (GDL) with a loading amount of 1 mg $cm^{-1}$.

**2.3. Characterization.** Scanning electron microscopy (SEM) images were acquired using a Hitachi SU-8010 ultrahigh-resolution scanning electron microscope with a resolution of 1.0 nm. Energy-dispersive X-ray spectroscopy (EDX) analysis was conducted by using an FEI Titan Cubed Themis microscope operated at 80 kV. Transmission electron microscopy (TEM) measurements were performed by using a JEOL 1400 microscope equipped with a 120 kV emission gun. X-ray photoelectron spectroscopy (XPS) measurements were carried out using Thermo Electron's ESCALAB 250 instrument, with the excitation source being the monochromatic Al K$\alpha$ line (1486.6 eV). The surface analyzed had a diameter of 500 $\mu$m. The high-pressure ion chromatography (HPIC) measurements were performed using a Thermo Fisher ICS6000 Chromatography system (column: BENSON BP-OA-2000-0, eluent: $H_2SO_4$ 0.05 N, flow rate: 0.4 mL $min^{-1}$, UV detection: 210 nm, temperature: ambient). X-ray absorption spectra (XAS) measurements at the Ag K-edges were conducted at the SOLEIL synchrotron SAMBA beamline,

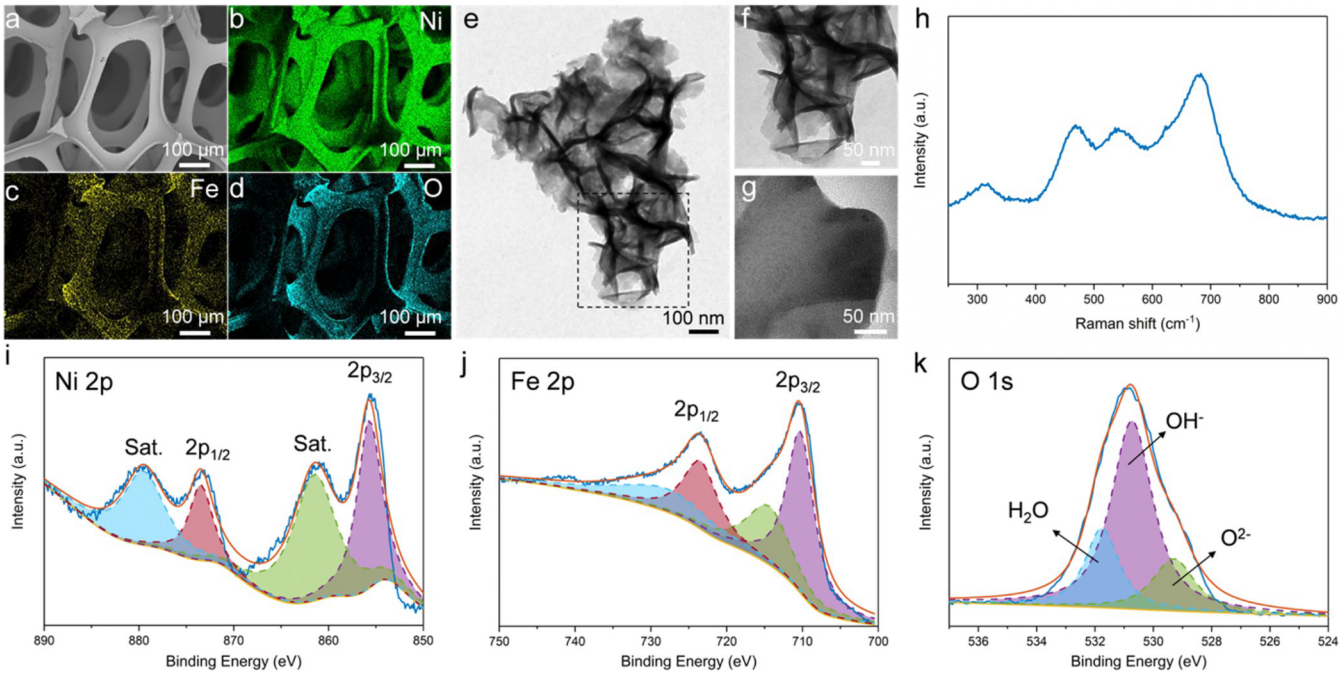


Figure 1. Characterizations of NiFe LDH electrodes. (a) Scanning electron microscopy (SEM) image and (b−d) energy-dispersive X-ray (EDX) elemental maps for NiFe LDH electrodes. (e−g) Transmission electron microscopy (TEM) images for NiFe LDH nanosheets. (h) Raman spectrum of NiFe LDH electrode. (i−k) X-ray photoelectron spectroscopy (XPS) results for NiFe LDH electrode.

which was equipped with a double-crystal Si(111) monochromator. The Ni and Fe K-edge XAS measurements were obtained at the XAS beamline of the Australian Synchrotron.

The samples were measured using fluorescence geometry and probed from ~150 eV below to ~800 eV above the edge. The Ni and Fe L-edge near-edge X-ray fine structure spectroscopy

(NEXAFS) measurements were obtained at the SXR beamline of the Australian Synchrotron under ultrahigh-vacuum conditions. The hard X-ray data were processed and modeled using the Demeter XAS software package (Athena and

Artemis), and the soft X-ray data are processed using the QANT procedure on Igor Pro. For EXAFS modeling, the reported structure of α-NiFe LDH was used to generate Ni−O, Fe−O, Ni−Fe(Ni), and Fe−Ni(Fe) contributions. $S_0^2$ values for Fe (0.79) and Ni (0.80) were obtained by modeling

the EXAFS of reference Fe and Ni foils, respectively. The fitting of the O K-edge is done by using the XPS peak software.

**2.4. Operando Raman Spectroscopy Measurement.** Operando Raman spectroscopy was performed by using a Renishaw inVia Raman microscope equipped with a 532 nm excitation source. The system was integrated with an optical microscope equipped with a long-working-distance 50× objective to focus the laser on the working electrode surface. The spectrometer was calibrated using a Si internal reference at 520.7 $cm^{-1}$ prior to the measurements.

An operando electrochemical cell was used, consisting of a NiFe LDH-coated carbon paper as the working electrode, a Pt wire as the counter electrode, and an Ag/AgCl (saturated KCl) reference electrode. The electrolyte solution was 0.5 M KOH, 0.5 M CsOH, and 0.5 M CsOH + 0.5 M EG. Operando Raman spectra were recorded at a potential range from the open circuit potential (OCP) to 1.7 V vs reversible hydrogen

**2.5. Faradaic Efficiency (FE) and Electric Power Consumption (EPC) Calculations.** The FE of gas products was determined by using the following formula:

$$FE_{gas} = g_i \times v \times \frac{z_i \times F \times P}{RT} \times \frac{1}{I_{total}} \times 100\% \quad (1)$$

The FE of liquid products was determined using the following formula:

$$FE_{liquid} = l_i \times \frac{z_i \times F}{Q_{total}} \times 100\% \quad (2)$$

The EPC was determined using the following formula:

$$EPC = \frac{E_{cell} \times z_i \times F}{}$$

$$\text{FE} \times V_m \quad (3)$$

where $g_i$ is the volume fraction of gas product $i$; $v$ is the gas flow rate; $z_i$ is the electron numbers for producing one molecule of product $i$; $I_{total}$ is the total current; $l_i$ is the mole numbers of liquid product $i$; $Q_{total}$ is the total charge passed during the reaction; and $E_{cell}$ is the cell voltage of product $i$. Additionally, the calculations involve constants such as $P$ (1.01 × $10^5$ Pa), $T$ (273.15 K), $F$ (96,485 C $mol^{-1}$), $R$ (8.314 J $mol^{-1}$ $K^{-1}$), and $V_m$ (22.4 L mol).

electrode (RHE) using an EmStat4S potentiostat (PalmSens).

**2.6. Electrochemical Active Surface Areas (ECSA) Measurement.** ECSA was measured by cyclic voltammetry (CV) at potentials −0.05 to 0.05 V (vs Ag/AgCl) with various scan rates of 20, 40, 60, 80, and 100 mV $s^{-1}$. The reaction area of the samples was fixed at 1 $cm^2$, and continuous Ar gas was fed. The double-layer capacitance ($C_{dl}$) was calculated by using the following equation:

$$C^{dl} = \frac{j_{nF}}{v} = \frac{j_a - j_c}{2v} \quad (4)$$

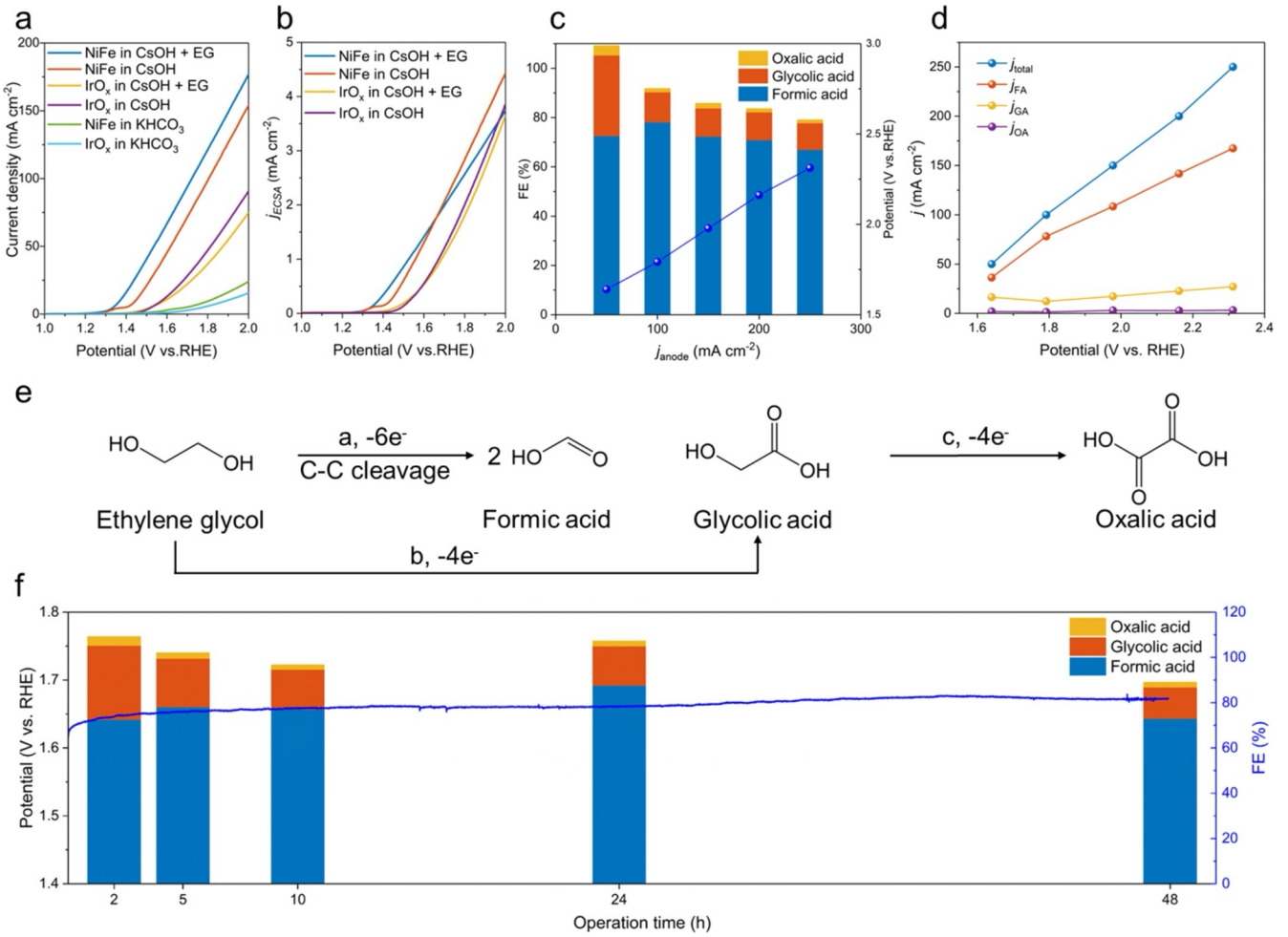


Figure 2. Electrocatalytic performance of EGOR. (a) Linear sweep voltammetry (LSV) curves and (b) ECSA-normalized LSV curves in different conditions. (c) Faradaic efficiencies of FA, GA, and OA at different current densities. (d) Partial current densities of the FA, GA, and OA. (e) Formation of FA, GA, and OA from the EGOR process. (f) EGOR performance of NiFe LDH at a current density of 50 mA $cm^{-2}$ over 48 h.

where $j_{nF}$ is the non-Faraday current density, equivalent to one-half of the value of the difference in anode current density ($J_a$) and cathode current density ($j_c$); $v$ is the different scan rate; and $C_{dl}$ is the slope of the line fitted to $j_{nF}$ at different scan rates.

The electrochemical surface area (ECSA) was calculated using the following equation (5), assuming a specific capacitance (Cs) of 0.04 mF $cm^{-2}$ in alkaline solution:

$$\text{ECSA} = \frac{C_{dl}}{C_s} \tag{5}$$

**2.7. Electrochemical Impedance Spectroscopy (EIS) Measurement.** The EIS was tested in 0.5 M $KHCO_3$ or 0.5 M CsOH + 0.5 M EG electrolytes at currents of 100, 250, and 500 mA, respectively, at frequencies from 100 kHz to 0.1 Hz and amplitudes of 5 mA.

**2.8. *iR* Compensation Measurement.** The linear sweep voltammetry (LSV) after *iR* compensation was plotted as a function of $j_{CO}$ versus $E_{cell\text{-}iR}$. The $E_{cell\text{-}iR}$ was calculated using the following equation:

$$E_{cell\text{-}iR} = E_{cell} - iR_e \tag{6}$$

where $E_{cell}$ is the cell voltage of the MEA cell and $R_e$ is the internal resistance, which was obtained by fitting the high-frequency region at different currents (Table S5). In this study, we used the $R_e$ tested under 250 mA, which is the smallest current we tested in MEA electrolyzer.

## 3. RESULTS AND DISCUSSION

**3.1. Characterization of the Synthesized NiFe LDH Anode Electrodes.** Iridium and ruthenium are widely used as anode catalyst for the OER,[14−16] but the broad-scale industrial utilization of these metals is impeded by their prohibitive cost. In a contrasting approach, the utilization of NiFe layered double hydroxide (NiFe LDH) as a catalyst has emerged due to its Earth-abundant composition, presenting a more economically viable alternative. NiFe LDH has been proven to exhibit high selectivity in the oxidation of organic substrates, leading to the production of value-added products in the organic oxidation reaction (OOR), while sustaining high current densities during its operation.[17,18] In our work, we electrodeposited NiFe LDH as a catalyst on a Ni foam substrate with a Ni/Fe precursor ratio of 1:1 (see the Supporting Information for details). For comparison, NiFe LDH was also grown on Ni foam via a hydrothermal reaction (Figure S1). Scanning electron microscopy (SEM) in Figure 1a showed the rough surface of the as-prepared NiFe LDH

electrode after deposition, which contrasts with the smooth surface of Ni foam before deposition (Figure S2). We performed energy-dispersive X-ray (EDX) mapping to confirm

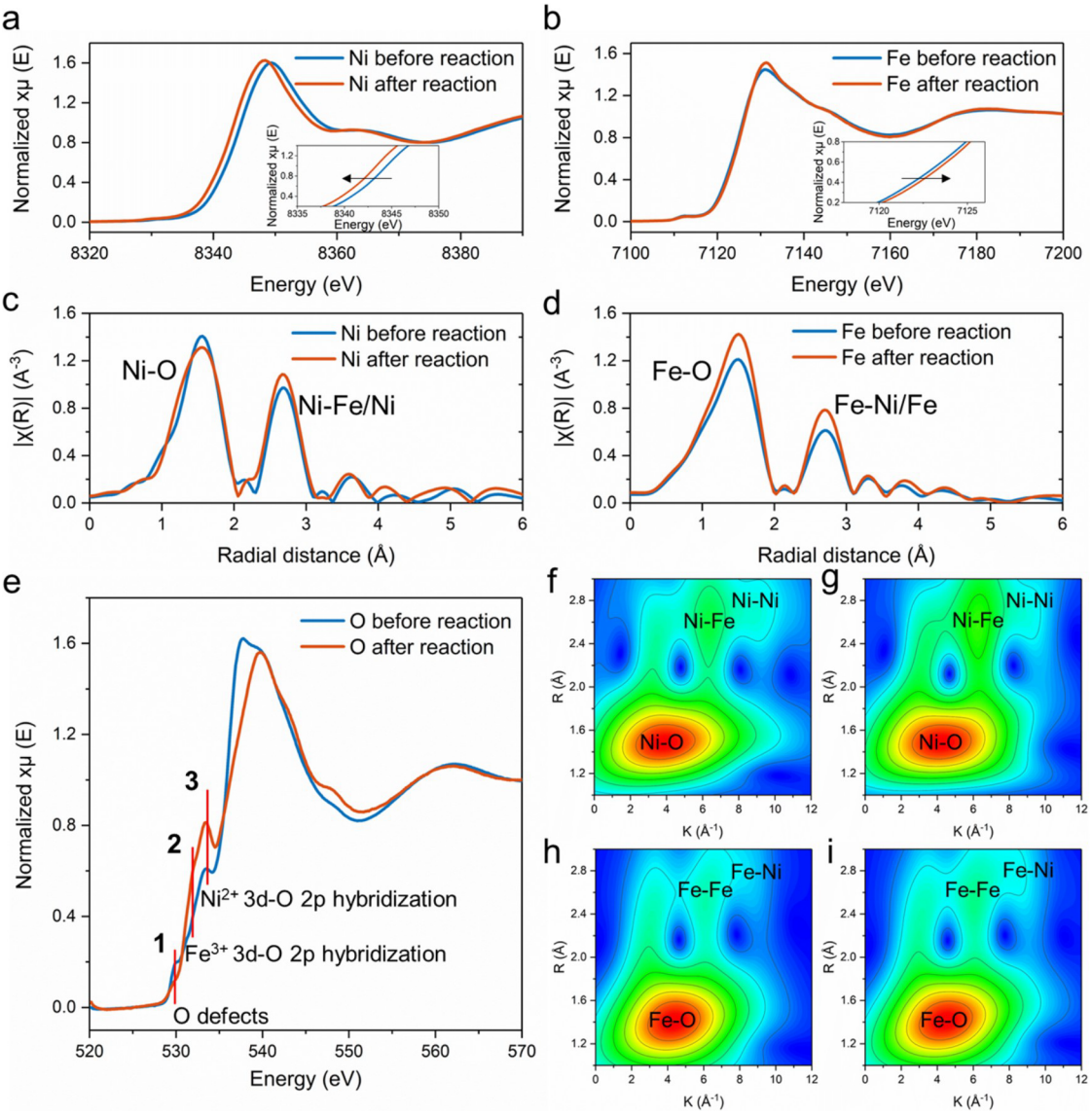


Figure 3. X-ray absorption spectroscopy (XAS) studies on NiFe LDH before and after 24 h EGOR. XANES spectra of (a) Ni K-edge and (b) Fe K-edge for the NiFe LDH before and after reaction. Fourier transform EXAFS spectra of (c) Ni K-edge and (d) Fe K-edge for the NiFe LDH before and after reaction. (e) O K-edge XAS spectra of NiFe LDH before and after EGOR. Wavelet transforms (WT) of the $k^3$-weighted EXAFS signals of Ni K-edge and Fe K-edge before (f, h) and after (g, i) 24 h at 100 mA $cm^{-2}$.

the uniform distribution of Fe and O elements on the Ni foam substrate (Figure 1b–d). Transmission electron microscopy (TEM) images (Figure 1e) revealed typical homogeneously curled NiFe LDH nanosheets indicative of a larger surface area. A magnified view of the highlighted region is shown in Figure 1f, while Figure 1g shows typical LDH lattice fringes. The intrinsic vibration details were investigated by Raman technology (Figure 1h), which shows the Ni–O and Fe–O vibrations. To further confirm the growth of NiFe LDH, we analyzed the surface compositions and chemical states of the NiFe LDH samples by using X-ray photoelectron spectroscopy (XPS) (Figure 1i–k). The results showed clear signals corresponding to Ni, Fe, and O elements, with no indications of other impurities. The Ni 2p spectrum in Figure 1i exhibited spin–orbit doublets at 855.5 and 873.4 eV (Ni $2p_{3/2}$ and Ni $2p_{1/2}$, respectively) along with two satellite peaks at 861.2 and 879.6 eV, indicating the presence of $Ni^{2+}$ ions and $Ni^{3+}$ in the NiFe LDH samples. The Fe 2p spectrum of NiFe LDH revealed two distinct peaks located at 710.6 and 723.7 eV, corresponding to Fe $2p_{3/2}$ and Fe $2p_{1/2}$, respectively (Figure 1j). Additionally, their corresponding satellite peaks at 714.9 and 728.8 eV confirm the presence of $Fe^{3+}$ ions. The O 1s spectrum in Figure 1k showed three peaks at 529.3, 530.7, and 531.8 eV, corresponding to $O^{2-}$, $OH^-$, and adsorbed water, respectively. Notably, the significant presence of the peak attributed to $OH^-$ confirmed that the hydroxide is the primary form in the as-prepared NiFe LDH samples. We then investigated the electrochemical behavior of both the deposited NiFe LDH and the Ni foam substrate, comparing them with those of deposited $IrO_x$/Ti and Ti mesh alone. The preparation of $IrO_x$ was based on our group's previously published methods.[19] To determine the double-layer capacitance ($C_{dl}$), we conducted cyclic voltammetry in the range of 850–950 mV versus the reversible hydrogen electrode (RHE) in 0.5 M CsOH with and without 0.5 M EG (Figures S3 and S4). Our findings reveal that in 0.5 M CsOH and 0.5 M EG,

NiFe LDH demonstrates the highest double-layer capacitance ($C_{dl}$) value, reaching 1.89 mF cm$^{-2}$ (Figure S5). We evaluated the roughness ratio ($R$) for each anode by dividing the $C_{dl}$ of the supported catalyst by the $C_{dl}$ of the substrate (i.e., the Ni foam or the Ti mesh) for each electrolyte (Figure S6). Notably, NiFe LDH exhibited significantly high $R$ values in the presence of EG, suggesting the activation of additional active sites for EG. This indicates the presence of selective sites on the surface of NiFe LDH, potentially contributing to its enhanced performance. Conversely, in the case of $IrO_x$, the values of $R$ remained independent of the presence of EG, suggesting that the enhanced performance originates from the NiFe LDH.

To assess the electrocatalytic performance of NiFe LDH toward the EGOR, we first performed the linear sweep voltammetry (LSV) in different electrolyte environments (Figure 2a). Compared to other electrodes and electrolytes, NiFe LDH demonstrated enhanced current density and a lower onset potential in 0.5 M CsOH + 0.5 M EG electrolyte. ECSA-normalized LSV curves were obtained, as shown in Figure 2b. To determine the selectivity of the involved electrochemical process, the geometrical current density of the anode was held for 2 h and the products were collected and analyzed using high-pressure ion chromatography (HPIC). The Faradaic efficiency was determined at increasing anodic current density from 50 to 250 mA cm$^{-2}$ (Figure 2c). Our analyses revealed that the main products of EGOR were formic acid (FA), glycolic acid (GA), and oxalic acid (OA) with average Faradaic efficiencies of approximately 72 ± 4, 16 ± 9, and 2 ± 1%, respectively. The identification of these reaction products is consistent with previous reports.[20,21] It is worth noting that as the current density increases, the total Faradaic efficiency for the EGOR decreases from 105 to 80%. This phenomenon can be attributed to the escalating competition between the OER and EGOR processes, which increases at larger overpotentials. The substantial Faradaic efficiency observed for both formic acid and glycolic acid is reflected in significant partial current densities, as graphically depicted in Figure 2d. Remarkably, out of the 8 potential products of EGOR involving electrons ranging from 2 up to 10, NiFe LDH displays a high degree of selectivity toward just 2 major products, each requiring 6 and 4 electrons. Based on the analysis of the products, we were able to elucidate the oxidation pathway for EGOR under alkaline conditions (Figure 2e). The first pathway involves 6 and 4 electrons and leads to the formation of formic acid via the cleavage of the C−C bond (pathway a) and glycolic acid (pathway b). The second main pathway for the EGOR on NiFe LDH is based on an 8 electron transfer to form oxalic acid as residual product of the reaction (pathway c).

We then gauged the stability of the catalyst by continuously testing it at a current density of 50 mA cm$^{-2}$. Figure 2f shows the evolution of the current density and the FE over a 48 h period. NiFe LDH exhibited stable performance, retaining 73 and 14% of the FE for formic acid and glycolic acid, respectively. Interestingly, we found that the Faradaic efficiency of formic acid remains virtually unchanged, while the Faradaic efficiency for glycolic acid decreases by approximately 20%. This decline can be attributed to the reduced concentration of ethylene glycol after prolonged operation and the higher selectivity for the formation of formic acid. The overall robust stability of the catalytic activity is further accompanied by a high stability of the catalyst structure and composition. Postmortem characterization, facilitated by EDX mapping, unveiled the uniform elemental distribution within the sample, underscoring the absence of metal aggregation during the electrooxidation process (Figure S7).

**3.2. Identification of the Structural Evolution of NiFe LDH during the OER and EGOR Processes.** To get further insight into the correlations between local atomic structure and the enhanced EGOR activity, we then performed X-ray absorption spectroscopy (XAS) studies on NiFe LDH before and after 24 h EGOR (Figure 3).[22−24] The X-ray absorption near-edge structure (XANES) spectra of the Ni K-edge (Figure 3a) showed a negative shift after reaction, which can be associated with a reduced oxidation state of Ni. The Fe K-edge, on the other hand (Figure 3b), exhibited a slight increase in white line intensity after the reaction, suggesting minimal changes in the electronic structure of Fe. Similarly, the features in the spectra of the Ni or Fe L-edge also indicated similar trends in electronic and oxidation state. In NiFe-LDH, both nickel and iron cations exhibit octahedral coordination with oxygen atoms, resulting in orbital splitting into the $t_{2g}$ and $e_g$ states. In the spectra of Ni L-edge (Figure S8), the decrease of $t_{2g}/e_g$ peak intensity in the $L_3$ region suggested a reduced oxidation state of Ni. Meanwhile, the spectra of Fe L-edge (Figure S9) demonstrate slight shift to higher energy in the $L_3$ region, suggesting an increased oxidation state of Fe. These results were consistent with the Ni K-edge and Fe K-edge, collaboratively suggesting possible electron transfer between Fe and Ni in the postreaction NiFe LDH. Conversely, the XPS spectrum after EGOR (Figure S10), Ni $2p_{3/2}$, and Ni $2p_{1/2}$ decreased while the two satellite peaks increased, indicating the reduction of $Ni^{2+}$ and the enhancement of $Ni^{3+}$, which could be attributed to the surface oxidation of the NiFe LDH, wherein the total oxidation state of Ni reduced as shown in XANES, which measures the bulk of the catalyst. Our investigations point to a possible electron transfer from Fe to Ni. Next, we examined the coordination environments of Ni and Fe using the Fourier transform EXAFS spectra (Figure 3c,d). The corresponding parameters and fits are shown in Tables S1 and S2 and Figures S11 and S12. Interestingly, the coordination number (CN) of the first shell Ni−O increased from 5.82 ± 0.15 to 6.65 ± 0.30 (Table S1) while that of the first shell Fe−O increased from 6.18 ± 0.68 to 6.52 ± 0.86 (Table S2). The observed increase in CN for M−O bonds may be partially attributed to the formation of a hydration layer or the adsorption of reactants/products.[24] However, these species are unlikely to persist in postreaction samples for an extended period. Therefore, we propose that the increase in CN is also influenced by a decrease in the number of oxygen vacancies. The pre-edge region of the O K-edge is considered a crucial indicator for assessing interaction between TM 3d and O 2p orbitals, as well as the existence of oxygen vacancies.[25,26] As shown in Figure 3e, weaker feature 1 suggests decreased density of oxygen vacancies in the postreaction NiFe LDH, which is consistent with the above fitting results of Ni and Fe K-edge EXAFS. Notably, the intensity of feature 1 is proportional to the number of oxygen vacancies, by fitting the O K-edge features (Figures S13 and S14), we quantified that the area of the fitted peak 0, located at feature 1, decreases from 0.427 to 0.298 (Tables S3 and S4), which again provides indirect evidence for a smaller quantity of oxygen vacancies. Further, the increased intensity of the pre-edge features 2 and 3 of the O K-edge after EGOR suggested an increased hybridization of Ni and Fe with nearby oxygens. As a

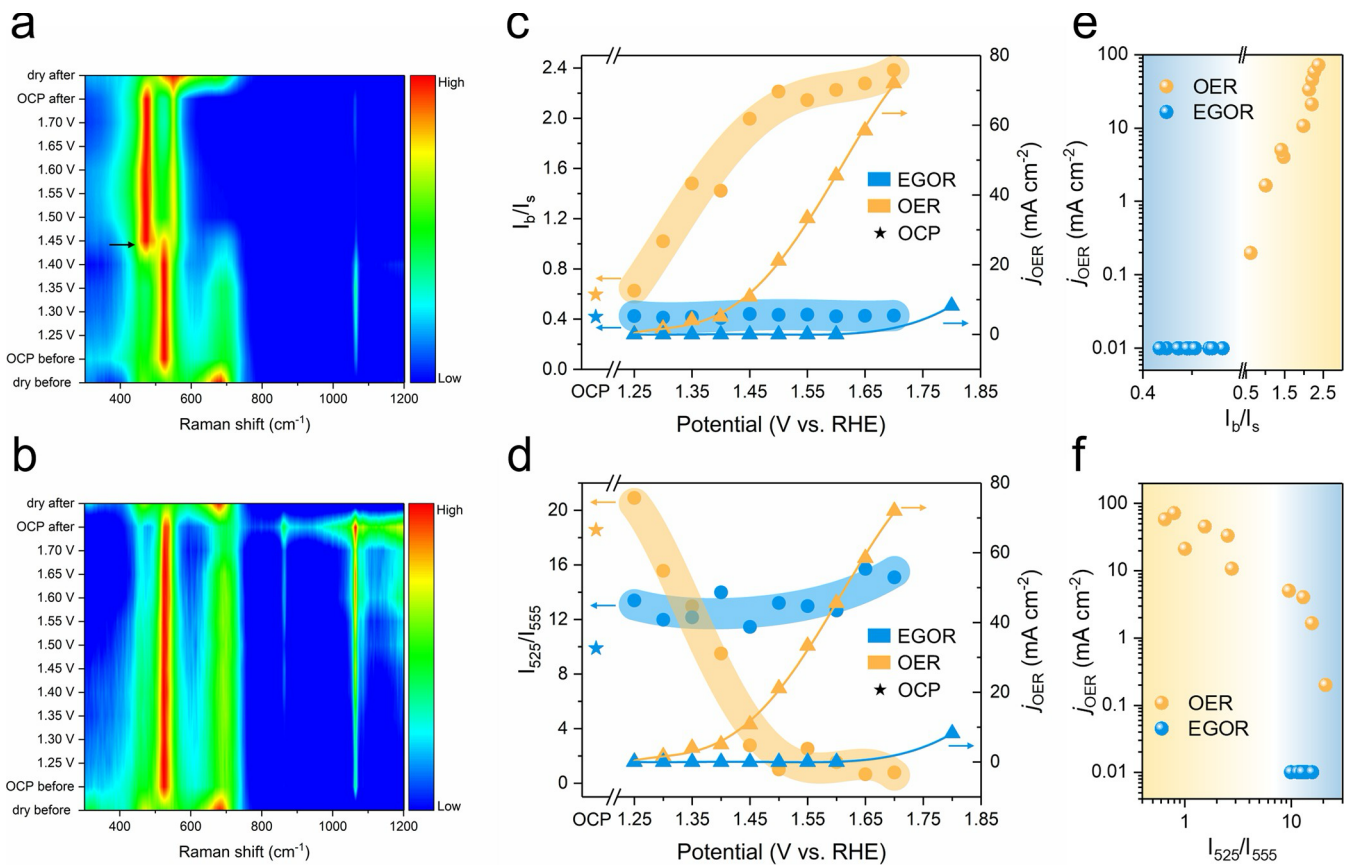


Figure 4. Operando Raman spectroscopy studies of the OER and EGOR using NiFe LDH as a catalyst. Operando Raman spectroscopy contour plots were conducted over a potential range from drying to the OCP conditions to 1.70 V vs RHE during the aforementioned OER (a) and EGOR (b). (c) Relative intensities of the $I_b$ and $I_s$ bands, along with the $j_{OER}$, as a function of potential during the OER and EGOR reactions. (d) Relative intensities of the 525 and 555 $cm^{-1}$ bands, along with the $j_{OER}$, as a function of potential during the OER and EGOR reactions. $j_{OER}$ as a function of (e) the $I_b/I_s$ ratio and (f) the $I_{525}/I_{555}$ ratio during the OER and EGOR reactions.

comparison, O K-edge spectra before and after the OER were also acquired (Figures S15−S17 and Tables S5 and S6). Notably, a clear increase in oxygen vacancies (feature 1) and a decrease in Fe and Ni hybridization (features 2 and 3) were observed after the OER. This behavior is in sharp contrast to the trend observed under EGOR conditions, thereby providing further support for our conclusion. The CN of the second shell Ni−Fe (Ni) increased from 4.24 ± 0.21 to 5.73 ± 0.43, while the Fe−Ni (Fe) increased from 3.68 ± 1.04 to 4.04 ± 1.07, demonstrating fewer metal vacancies from Ni or Fe after EGOR, which is attributed to the enhancement of metal−oxygen hybridization during the EGOR. We note that the observed increase in M−M CN is unlikely to indicate particle aggregation, as it primarily reflects local coordination changes rather than large-scale structural reorganization.[27,28] This is further supported by postreaction TEM images (Figure S18), which showed no evidence of NiFe LDH aggregation. Notably, although the second-shell coordination numbers (CNs) of Ni−Fe(Ni) and Fe−Ni(Fe) are ideally expected to be similar due to the averaged nature of EXAFS fitting, our measurements revealed subtle, yet consistent, differences (Tables S1 and S2). Specifically, the Ni−Fe(Ni) CN was 4.24 ± 0.21, while the Fe−Ni(Fe) CN was 3.68 ± 1.04. These deviations likely originate from local structural asymmetries and disorder, such as nonuniform elemental distribution, preferential edge-site occupation by Fe, and variations in short-range ordering—particularly under nonideal Ni/Fe stoichiometries.[29−31] Furthermore, the larger uncertainty associated with the Fe−Ni fit suggests reduced signal-to-noise ratio or higher structural variability around Fe sites, which can bias the extracted CNs. While the Ni−Fe and Fe−Ni paths are crystallographically symmetric, the EXAFS-derived CNs can diverge due to the sensitivity of the fit to such local heterogeneities.

The unchanged Ni−O, Ni−Fe, Fe−O, and Fe−Ni bond lengths further corroborate that the as-prepared NiFe LDH maintains structural stability even after long-term EGOR (Tables S1 and S2). The Ni K-edge and Fe K-edge wavelet transform (WT) contour maps both show two hot spots at high K spaces at 2.7 Å, suggesting the coexistence of Ni and Fe at this distance (Figure 3f−i), further validating the structural stability and homogeneous metal distribution before and after long-term reaction. The WT contour map further confirmed the increase of Ni−Fe and Fe−Ni coordination peak intensity, which is consistent with the previous results. Collectively, these results suggest that NiFe LDH undergoes low defect creation during the EGOR process. We attribute this behavior to the enhanced hybridization of metal−oxygen, thereby allowing the NiFe LDH to maintain a stable structure. Remarkably, our investigations reveal that the behavior of NiFe LDH during EGOR differs significantly from that during OER, which is typically accompanied by the formation of a large number of vacancies that increase the number of active sites.[26,32−34]

Next, we conducted operando Raman spectroscopy on NiFe LDH under the OER and EGOR conditions. We focused on

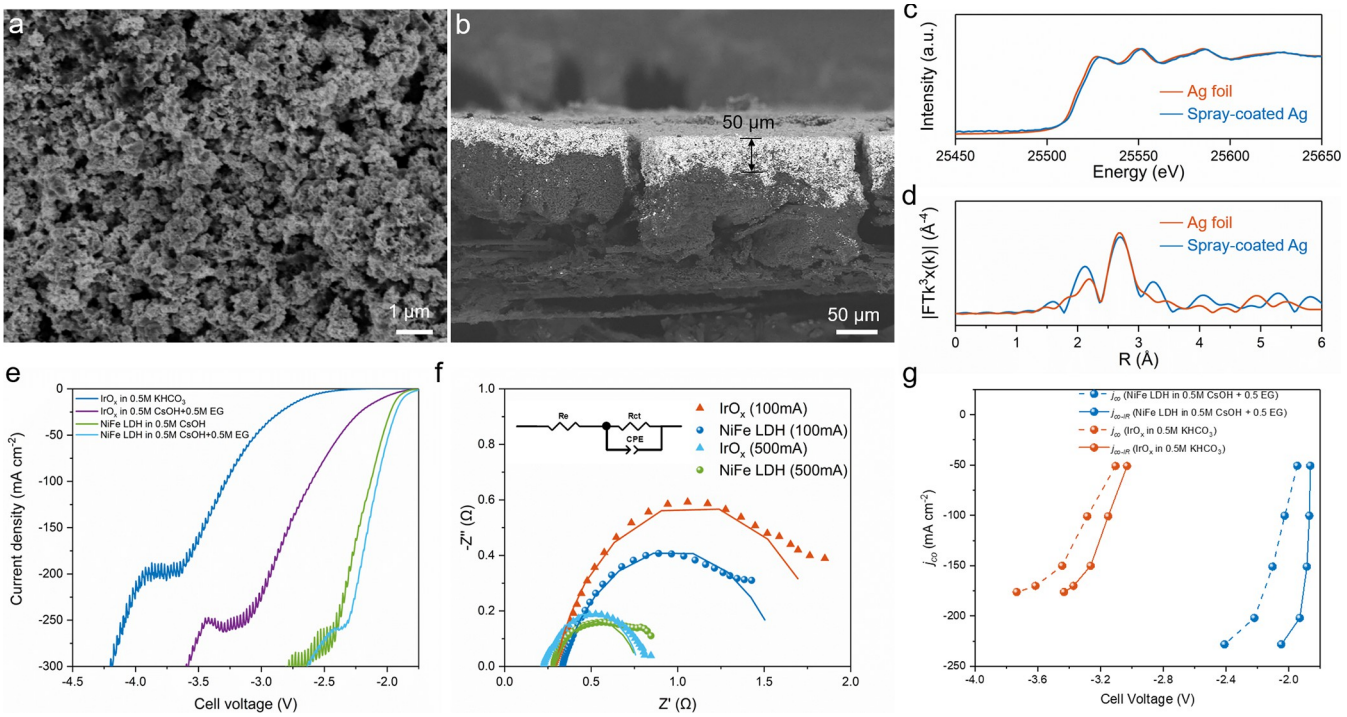


Figure 5. Electrochemical characterization of the $CO_2$RR-EGOR system using Ag-NPs as cathode catalyst in MEA electrolyzer. (a) SEM image of the Ag-NPs deposited on the gas diffusion electrode and (b) the corresponding cross-sectional SEM image. (c) Ag K-edge XANES spectra and (d) the corresponding Fourier transform EXAFS spectra of Ag-NPs and Ag foil used as reference. (e) LSV of the $CO_2$RR-EGOR system in MEA electrolyzer, using $IrO_x$, NiFe LDH as catalysts and 0.5 M $KHCO_3$, 0.5 M CsOH, and 0.5 M CsOH + 0.5 M EG as electrolyte. (f) Nyquist plots of the $CO_2$RR-OER system and the $CO_2$RR-EGOR system at different current densities (solid symbols are experimental results and solid lines are fitting results). (g) $j_{CO}$ as a function of cell voltage before (dashed lines) and after (solid lines) *iR* compensation.

Raman bands between 300 and 1200 $cm^{-1}$, examining changes as the applied potential increased from drying to open circuit potential (OCP) to 1.70 V vs RHE (Figures 4a,b, S19 and S20). The Raman spectra were found to be nearly identical in both electrolytes, with only a slight peak at 862 $cm^{-1}$ observed in the presence of ethylene glycol. However, in the range 1000−1200 $cm^{-1}$, additional peaks were detected under EGOR conditions that were not apparent under the OER conditions. These peaks, located at 1064.1 and 1084.8 $cm^{-1}$, are attributed to carbonate ($CO_3^{2-}$) and bicarbonate ($HCO_3^-$) species, respectively. Their presence suggests that ethylene glycol facilitates the absorption of $CO_2$ from ambient air by CsOH at the gas−liquid interface, promoting the formation of these carbonate species. This effect is likely enhanced by the vigorous interfacial mixing during EGOR. In contrast, under the OER conditions, the generation of $O_2$ may hinder $CO_2$ uptake from air, resulting in much weaker or absent signals for carbonate-related species. Deconvolution of the spectra revealed bands in the 400−600 $cm^{-1}$ range, corresponding to Ni−O and Fe−O vibrations, along with a prominent peak at 715 $cm^{-1}$ attributed to β-FeOOH.[35] Distinct differences emerged between OER and EGOR at potentials near the OER onset value of 1.45 V vs RHE. Under OER conditions, as the voltage reaches the onset potential, the peaks abruptly shift from 460 $cm^{-1}$ and 525 to 478 and 555 $cm^{-1}$, respectively, which is a characteristic phenomenon of NiFe LDH during OER. These two emerged bands correspond to the Ni−O bending ($I_b$) and stretching ($I_s$) vibrations of NiOOH, respectively—in line with the literature.[36] The intensity of the 478 $cm^{-1}$ band increased significantly, which is attributed to NiOOH formation within NiOOH-NiFe LDH hybrids,[35] while the 460 $cm^{-1}$ signal arose from Ni−O vibrations in $Ni(OH)_2$.[35] These changes suggest the transformation of $Ni(OH)_2$ into NiOOH-NiFe LDH hybrids during OER. The disappearance of the 715 $cm^{-1}$ peak aligns with the instability of β-FeOOH in the electrolyte, as previously reported in the literature.[35] We also compared the catalyst behavior in KOH and CsOH under the OER and found comparable signals (Figures S19−S22).

Conversely, during EGOR, the sharp band at 525 $cm^{-1}$, attributed to Ni−O bending in $Ni(OH)_2$, emerged rapidly under the OCP conditions and then remained stable. Our data show that the peak ratio of 478−525 $cm^{-1}$ increased linearly under the OER, whereas it remained constant during the EGOR (Figure S23). This finding confirms that the 478 $cm^{-1}$ signal during the OER originates from NiOOH-NiFe LDH heterostructures, emphasizing their role in the OER activation, as suggested in earlier studies.

To further investigate these structural changes, we plotted the relative intensities of the 478 and 555 $cm^{-1}$ peaks ($I_b/I_s$) (Figure 4c,e). Interestingly, the $I_b/I_s$ ratio increased during OER activation but remains stable under EGOR, indicating diverging structural evolutions of NiFe LDH. During the OER process, the change in $I_b/I_s$ and the disappearance of the 715 $cm^{-1}$ peak from β-FeOOH suggest that $Ni^{2+}$ in $Ni(OH)_2$ may be replaced by $Fe^{3+}$ from β-FeOOH, establishing a dynamic equilibrium, with Fe content gradually decreasing as the voltage increases.[37] However, after drying the sample post-OER, we observe a reemergence of the 715 $cm^{-1}$ peak, albeit with reduced intensity, indicating a partially reversible process (Figure S19).

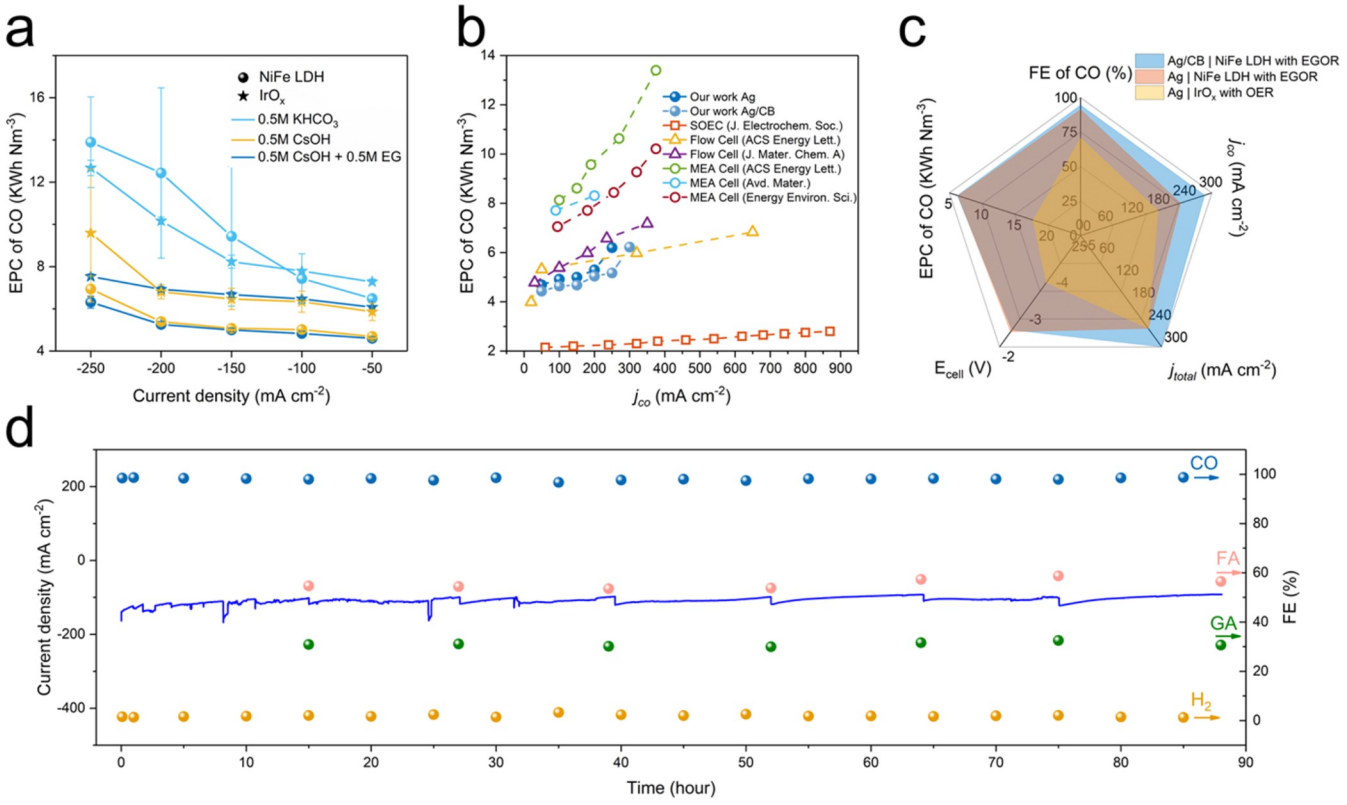


Figure 6. Investigation of the energy consumption performance analysis for $CO_2$RR-EGOR system. (a) EPC of $CO_2$RR-EGOR system and $CO_2$RR-OER system in 0.5 M $KHCO_3$, 0.5 M CsOH, and 0.5 M CsOH + 0.5 M EG as electrolytes (spheres represent NiFe LDH, stars represent $IrO_x$). (b) Comparison of the EPC metrics with previous literature benchmarks based on MEA electrolyzers, flow cells, and solid oxide electrolysis cells (SOEC). (c) Comparison of the performance metrics of the MEA electrolyzers based on the $CO_2$RR-OER system and the $CO_2$RR-EGOR system. The current density is taken as an absolute value. (d) $CO_2$RR-EGOR system performance at a cell voltage of 2.05 V over ~90 h.

We also examined the evolution of the 525 and 555 $cm^{-1}$ peaks, corresponding to Ni−O bending in $Ni(OH)_2$ and NiOOH, respectively (Figure 4d,f). A strong correlation was observed between the OER current density ($j_{OER}$) and a decrease in the $I_{525}/I_{555}$ ratio, signifying the conversion of $Ni(OH)_2$ to NiOOH. Conversely, under EGOR, the $I_{525}/I_{555}$ ratio remained high, suggesting a higher proportion of $Ni(OH)_2$ relative to NiOOH in NiFe LDH.

Taken together, these results from Raman and XAS analyses reveal distinct structural evolutions of NiFe LDH during the OER and EGOR processes. Under OER conditions, NiFe LDH undergoes significant changes, including the irreversible conversion of $Ni(OH)_2$ to NiOOH forming NiOOH-NiFe LDH heterostructures together with the creation of oxygen vacancies. In contrast, EGOR induces metal−oxygen hybridization, as corroborated by the increased Raman signals for $Ni(OH)_2$ and the absence of heterostructure formation. Such hybridization stabilizes the NiFe LDH structure, creating selective active sites for EGOR while minimizing the defective structures associated with the OER activity.

**3.3. Pairing $CO_2$RR and EGOR Using Ag-NPs as Cathode Catalyst in MEA Electrolyzer.** To evaluate the synergistic effects of EGOR on $CO_2$RR, we integrated the NiFe LDH anode into a 5 $cm^2$ MEA electrolyzer and investigated the coelectrolysis of $CO_2$ and EG. Ag nanoparticles (Ag-NPs) were used as a cathode catalyst for the conversion of $CO_2$ to CO owing to the fact that Ag is a very selective catalyst and CO product can be easily separated from hydrogen, while the gaseous products can prevent the liquid contamination to the anode. In our study, we selected CsOH + EG as the anolyte. Previous reports have demonstrated that using a larger cation (e.g., $Cs^+$) in the anolyte, compared to smaller cations ($K^+$ or $Na^+$), can effectively enhance the partial current density for $CO_2$RR to CO.[38] We found that using KOH instead of CsOH in the $CO_2$RR-EGOR system led to a significant decrease in the Faradaic efficiency of CO at current densities above 200 mA $cm^{-2}$ (Figure S24). Additionally, KOH electrolyte required a higher voltage for electrolysis, which is consistent with previous findings.[39,40] To determine whether the difference originated from the anode or cathode, we also performed control experiments using KOH + EG for EGOR. The activity and selectivity were comparable to those with CsOH + EG (Figure S25), indicating that the alkali cation has little effect on EGOR under our conditions. Thus, the performance difference mainly stems from the impact of $Cs^+$ on $CO_2$RR. For the experiments, Ag-NPs were dispersed, forming an ink solution, and uniformly sprayed onto a carbon gas diffusion layer (GDL) (see details in Section 2). SEM images showed the uniform and porous surface of the coated Ag-NPs on the mesoporous surface of GDL (Figure 5a). Cross-sectional SEM of the cathode confirmed the homogeneous silver, with an average thickness of approximately 50 $\mu$m (Figure 5b). Ag K-edge X-ray absorption spectroscopy (XAS) was employed to analyze the structural characteristics and oxidation state of the spray-coated Ag, using Ag foil as a reference. Figure 5c shows that the normalized Ag K-edge X-ray absorption near-edge structure (XANES) spectrum of the spray-coated Ag exhibited oscillations, which match well with

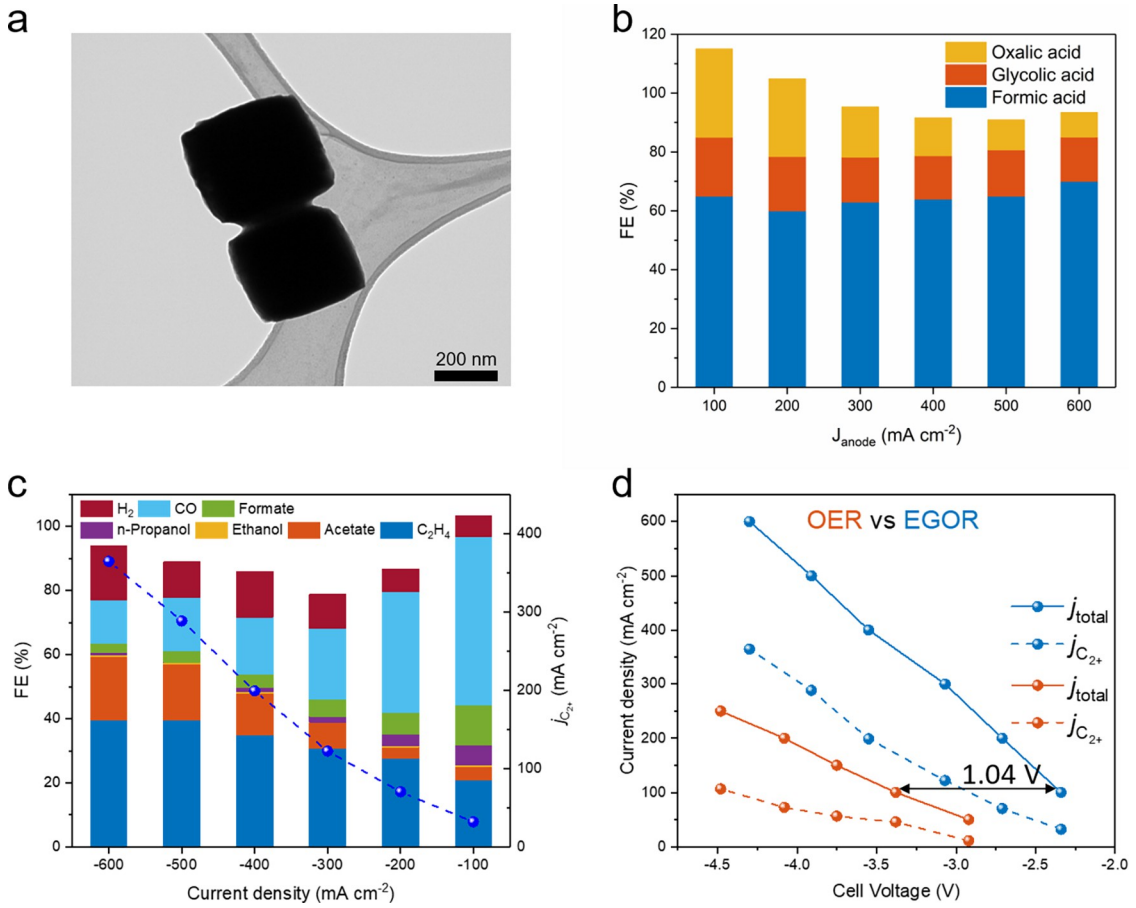


Figure 7. Electrochemical characterization of the $CO_2$RR-EGOR system using $Cu_2O$ as a cathode catalyst in a two-component electrolyzer. (a) TEM image of as-prepared $Cu_2O$. (b) Faradaic efficiencies of FA, GA, and OA at different current densities in a two-component electrolyzer. (c) Faradaic efficiency of $CO_2$ and the corresponding $C_{2+}$ partial current density in $CO_2$RR-EGOR system with $Cu_2O$ as cathode catalyst. (d) Comparison of cell voltage between the $CO_2$RR-EGOR system and the traditional $CO_2$RR-OER system using $Cu_2O$ as cathode catalyst.

that of the Ag foil, confirming the presence of metallic Ag without any additional changes in the oxidation state. This was further corroborated by the corresponding extended X-ray absorption fine structure (EXAFS) analysis in Figure 5d. It is worth mentioning that the positions and intensities of Ag-NPs shown in XANES almost coincide with those of Ag foil, suggesting that the Ag-NPs have a metal-like d-state density. The similarity of the EXAFS spectra suggested further indications that the local structures in the Ag-NPs are isostructural with that of the bulk Ag metal.[41]

We first used LSV analyses to explore the electrochemical response of the $CO_2$RR-EGOR system in the MEA electrolyzer (Figure 5e). Our results show that the NiFe-LDH anode outperforms $IrO_x$ as anode catalyst for both the $CO_2$RR-EGOR and the $CO_2$RR-OER configuration. At the same current density, the $CO_2$RR-EGOR system exhibits the lowest voltages compared to the traditional $CO_2$RR-OER system. Remarkably, the LSV curves are found smoother in the case of $CO_2$RR-EGOR compared to the case of $CO_2$RR-OER due to the strong suppression of the $O_2$ bubbles at the anode from the OER when using EG. We also found that the LSV curves do not show a monotonous increase of the current density when increasing the cell voltage. This observation, independent of the catalysts or the reaction at the anode, is attributed to enhanced hydrogen evolution reaction (HER) at high potentials and could originate from a limited diffusion of $CO_2$ at higher reaction rates (Figure S26). To further understand the charge transfer kinetics in the MEA electrolyzers, we recorded the electrochemical impedance spectra (EIS) of the $CO_2$RR-OER system and the $CO_2$RR-EGOR system at different current densities (Figure 5f). The Nyquist plots were collected between 100 kHz and 0.1 Hz, and the curves were fitted using the equivalent circuit presented in the inset of Figures 5f and S27. Our results show that the charge transfer resistance ($R_{ct}$) obtained from the Nyquist plots in the $CO_2$RR-EGOR system is smaller than that obtained in the $CO_2$RR-OER system, indicating a faster reaction rate. We used the values of the internal resistance ($R_e$) fitted from the Nyquist plot (Table S7) to correct the Ohmic drop (see the Supporting Information for details). Figure 5g shows the partial current densities of CO ($j_{CO}$) versus the full-cell potential with and without $iR$ compensation. After $iR$ compensation, we observed that a voltage below 2 V can be obtained for an industrial-relevant current density for CO of >220 mA $cm^{-2}$, which indicates that further improvement of the MEA is requested to further decrease the operating voltage.

To better assess the real-life performance of $CO_2$RR-EGOR system, the *iR* compensation was not considered in the rest of the manuscript.[42] We also scrutinized the different parameters associated with the conversion of $CO_2$ to CO such as the nature of the electrolyte, the type of membrane, and nature of the catalyst at the anode (Note 1 in the Supporting Information).

Electric power consumption (EPC) is a key parameter in the assessment of the economic viability of the $CO_2$RR process, given its substantial contribution to the operational expenditure (OPEX) associated with the process. We calculated the EPC of the $CO_2$RR-EGOR and $CO_2$RR-OER systems (see the Supporting Information for details) and found that the $CO_2$RR-EGOR system, employing NiFe LDH as the anode catalyst and Ag-NPs as the cathode catalyst, exhibits the lowest EPC (Figure 6a). Notably, the EPC for the $CO_2$RR-EGOR system remains relatively constant from 50 to 250 mA $cm^{-2}$, culminating at 6.2 kWh $Nm^{-3}$ at a current density of 250 mA $cm^{-2}$. Our results also compared favorably to previous literature benchmarks for the conversion of $CO_2$ to CO and suggest a potential economic potential (Figure 6b and Note 2). A thermodynamic energy efficiency analysis (Note 3) further reveals that although EGOR reduces the cell operating voltage, the overall energy efficiency at a current density of 150 mA $cm^{-2}$ is slightly lower than that of the conventional $CO_2$RR-OER system. Specifically, the efficiencies reach 22.7% for glycolic acid (GA) and 33.8% for formic acid (FA) as anodic products, compared to 39.2% for the OER-based system. This reduction stems from the additional chemical energy content of the anodic reactant, underscoring the inherent trade-offs in paired electrolysis design. We observed that the $CO_2$RR-EGOR system outperforms the previous MEA systems with a 39.4% reduction of the electrical power consumption at $\sim j_{CO}$ = 200 mA $cm^{-2}$. These results are also comparable to those of liquid flow cell electrolyzers. The improved EPC is attributed to the low cell voltage and high Faraday efficiency for CO. Figure 6c shows the performance metrics highlighting the superiority of the $CO_2$RR-EGOR system (indicated by the red trace) over the $CO_2$RR-OER counterparts. The metrics encompass current density, $FE_{CO}$ (Faradaic efficiency for CO), cell voltage, and EPC. Additionally, we found that incorporating a mixture of Ag and conducting carbon particles improves the charge transfer and can further improve the cathode performance. It results in a specific current density for CO of ~280 mA $cm^{-2}$, which constitutes a substantial 23% increase (indicated by the blue trace). This finding strongly advocates for future optimization via engineering of the ink formulation for the cathode.

We finally evaluated the stability of the $CO_2$RR-EGOR system by operating the MEA cell under a constant potential of 2.05 V with an average current larger than 100 mA $cm^{-2}$ (Figure 6d). After ~90 h, the Faradaic efficiency (FE) was estimated to be 99.3% for CO, 56% for FA, and 31% for GA, corresponding to retentions of approximately 100%.

**3.4. Electrochemical Characterization of the $CO_2$RR-EGOR System Using $Cu_2O$ as Cathode Catalyst in Two-Component Electrolyzer.** To generalize our approach of pairing $CO_2$RR and EGOR, we investigated the conversion of $CO_2$ to multicarbon products using $Cu_2O$ nanocubes as a cathode catalyst. To prevent liquid contamination of the liquid products from the cathode and anode, we designed a two-component electrolyzer, as shown in Figure S28. Specifically, we used 0.5 M CsOH as the catholyte and 0.5 M CsOH + 0.5 M EG as the anolyte, thereby eliminating the formation of a pH gradient across the membrane and avoiding the thermodynamic instability that typically arises from pH mismatch. The liquid products of the $CO_2$RR are retained in the catholyte, while the liquid products of the EGOR are retained in the anolyte, simplifying the subsequent separation of the liquid products from each other. Cubic-shaped $Cu_2O$ was synthesized with an average size of 400 nm (Figures 7a and S29). The corresponding XRD spectrum is shown in Figure S30. The electrochemical responses of the $CO_2$ electrolysis cells using OER and EGOR are presented in Figure S31. The $CO_2$RR-EGOR system exhibits lower cell potentials than does the $CO_2$RR-OER system at the same current density. As shown in Figure 7b, the EGOR remains stable at a current density up to 600 mA $cm^{-2}$, with average Faraday efficiencies of approximately 64.5% for formic acid, 16.6% for glycolic acid, and 17.5% for oxalic acid. At the cathode, we achieved an up to 60.7% Faraday efficiency of $C_{2+}$ at −600 mA $cm^{-2}$ with a partial current density of 364.44 mA $cm^{-2}$ (Figure 7c). As shown in Figure 7d, the $CO_2$RR-EGOR system using $Cu_2O$ as the cathode catalyst and NiFe LDH as the anode catalyst reduced the cell voltage by more than 1 V compared to the traditional $CO_2$RR-OER system, resulting in a 31% reduction in electricity consumption.

## 4. CONCLUSIONS

In summary, we propose a paired $CO_2$RR-EGOR system as an alternative to the traditional $CO_2$RR-OER system using NiFe LDH as the anode material. Using X-ray absorption spectroscopy and operando Raman spectroscopy investigations, we identified that NiFe LDH undergo profound and distinct structural changes under OER and EGOR conditions favoring selectivity of the reaction toward water or EG oxidation. As-prepared NiFe LDH maintained structural stability after EGOR, with an increased metal−oxygen hybridization offering selective active sites for the oxidation of hydroxy groups of EG. In contrast, the OER induced an irreversible structural evolution, where $Ni(OH)_2$ transformed to NiOOH, leading to the formation of NiOOH-NiFe LDH heterostructures. By utilizing the NiFe-LDH as the anode catalyst and Ag-NPs as the cathode catalyst in an MEA electrolyzer, we achieved a low full-cell voltage of 1.9 V and near 100% FE for CO production at a current density of 50 mA $cm^{-2}$ corresponding to a 1.3 ± 0.1 V decrease and 38 ± 2% reduction in electricity consumption. We also achieved a partial current density of 364 mA $cm^{-2}$ for $C_{2+}$ products with an $FE_{C_{2+}}$ of 61% using

$Cu_2O$ as a cathode catalyst. Paired electrolysis led to a reduced cell voltage of 1.04 V, equivalent to a 31% reduction in energy consumption for the production of multicarbon products. Our approach offers a simple strategy to reduce the energy consumption while enhancing the economic feasibility of the electrochemical conversion of $CO_2$.

## ASSOCIATED CONTENT

### *Supporting Information

The Supporting Information is available free of charge at https://pubs.acs.org/doi/10.1021/acscatal.5c02291.

Additional experimental data, electrochemical measure- ments, comparisons of anode catalyst, technoeconomic analysis, energy efficiency calculation, fitting parameters according to the Ni R-space and Fe R-space; fitting results of the O k-edge features before and after both EGOR and OER; fitting results of the EIS; market prices of all items; comparison of EPC and EE in the different electrolysis systems; smooth surface of Ni foam before deposition; determination of ECSA of OER and EGOR in different electrolytes; EDX mapping after reaction; XPS results after EGOR; TEM images of NiFe LDH

after EGOR; and SEM image of the as-prepared $Cu_2O$ catalyst (PDF)

## AUTHOR INFORMATION


### Corresponding Author

Damien Voiry − *Institut Européen des Membranes, IEM, UMR 5635, Université Montpellier, ENSCM, CNRS, Montpellier 34000, France;* orcid.org/0000-0002-1664-2839; Email: damien.voiry@umontpellier.fr

### Authors

Jiefeng Liu − *Institut Européen des Membranes, IEM, UMR 5635, Université Montpellier, ENSCM, CNRS, Montpellier 34000, France*

Yuwei Yang − *School of Chemical Engineering, University of New South Wales, Sydney, NSW 2052, Australia*

Eddy Petit − *Institut Européen des Membranes, IEM, UMR 5635, Université Montpellier, ENSCM, CNRS, Montpellier 34000, France*

Valérie Bonniol − *Institut Européen des Membranes, IEM, UMR 5635, Université Montpellier, ENSCM, CNRS, Montpellier 34000, France*

Zakaria Anfar − *Institut Européen des Membranes, IEM, UMR 5635, Université Montpellier, ENSCM, CNRS, Montpellier 34000, France*

Bertrand Rebiere − *Institut Européen des Membranes, IEM, UMR 5635, Université Montpellier, ENSCM, CNRS, Montpellier 34000, France*

Bonito Aristide Karamoko − *Institut Européen des Membranes, IEM, UMR 5635, Université Montpellier, ENSCM, CNRS, Montpellier 34000, France;* orcid.org/0009-0007-4171-5159

Wensen Wang − *Institut Européen des Membranes, IEM, UMR 5635, Université Montpellier, ENSCM, CNRS, Montpellier 34000, France;* orcid.org/0000-0003-4109-3103

Huali Wu − *Institut Européen des Membranes, IEM, UMR 5635, Université Montpellier, ENSCM, CNRS, Montpellier 34000, France*

Mathilde Moderne − *Institut Européen des Membranes, IEM, UMR 5635, Université Montpellier, ENSCM, CNRS, Montpellier 34000, France*

Robin Guéret − *Institut Européen des Membranes, IEM, UMR 5635, Université Montpellier, ENSCM, CNRS, Montpellier 34000, France*

Philippe Miele − *Institut Européen des Membranes, IEM, UMR 5635, Université Montpellier, ENSCM, CNRS, Montpellier 34000, France;* orcid.org/0000-0003-3530-8120

Nicholas M. Bedford − *School of Chemical Engineering, University of New South Wales, Sydney, NSW 2052, Australia;* orcid.org/0000-0002-4424-7094

Chrystelle Salameh − *Institut Européen des Membranes, IEM, UMR 5635, Université Montpellier, ENSCM, CNRS, Montpellier 34000, France*

Complete contact information is available at: https://pubs.acs.org/10.1021/acscatal.5c02291


### Author Contributions

D.V. conceived the idea, designed the experiments, and wrote the manuscript. J.L. designed the experiments with D.V., prepared the electrodes, and performed the electrochemical measurements. D.V. and J.L. analyzed the data and wrote the manuscript. Y.Y. assisted J.L. with the XAS measurements. V.B. carried out the high-performance liquid chromatography measurements. D.V. and B.R. carried out the scanning electron microscopy and the energy-dispersive X-ray mapping. Z.A. carried out the transmission electron microscopy. B.A.K., W.W., H.W., and M.M. assisted J.L. with the electrochemical measurements. R.G. assisted J.L. with the electrochemically active surface area and electrochemical impedance spectra measurements. C.S., N.M.B., and P.M. discussed the results with D.V. and J.L. All of the authors edited the manuscript before submission.

### Notes

The authors declare no competing financial interest.

## ACKNOWLEDGMENTS


D.V. and H.W. acknowledge funding from the European Research Council (ERC) under the European Union's Horizon 2020 research and innovation program (grant agreement no. 804320). J.L. and W.W. acknowledge PhD scholarship from the China Scholarship Council (CSC). N.M.B. and Y.Y. acknowledge partial financial support from the Faculty of Engineering at the University of New South Wales. Fe and Ni K-edge measurements were performed at the XAS beamline of the Australian Synchrotron, while O K-edge and Ni/Fe L-edge measurements were performed at the SXR beamline of the Australian Synchrotron, part of ANSTO. We would like to thank Dr. Jessica Hamilton at the XAS beamline and Dr. Bruce Crowie at the SXR beamline for their assistance with XAS measurements.


## REFERENCES


(1) Ozden, A.; García de Arquer, F. P.; Huang, J. E.; Wicks, J.; Sisler, J.; Miao, R. K.; O'Brien, C. P.; Lee, G.; Wang, X.; Ip, A. H.; Sargent, E. H.; Sinton, D. Carbon-efficient carbon dioxide electrolysers. *Nat. Sustainability* 2022, *5* (7), 563−573.

(2) Wakerley, D.; Lamaison, S.; Wicks, J.; Clemens, A.; Feaster, J.; Corral, D.; Jaffer, S. A.; Sarkar, A.; Fontecave, M.; Duoss, E. B.; Baker, S.; Sargent, E. H.; Jaramillo, T. F.; Hahn, C. Gas diffusion electrodes, reactor designs and key metrics of low-temperature CO2 electrolysers. *Nat. Energy* 2022, *7* (2), 130−143.

(3) De Luna, P.; Hahn, C.; Higgins, D.; Jaffer, S. A.; Jaramillo, T. F.; Sargent, E. H. What would it take for renewably powered electrosynthesis to displace petrochemical processes? *Science* 2019, *364* (6438), No. eaav3506.

(4) Xie, K.; Miao, R. K.; Ozden, A.; Liu, S.; Chen, Z.; Dinh, C.-T.; Huang, J. E.; Xu, Q.; Gabardo, C. M.; Lee, G.; Edwards, J. P.; O'Brien, C. P.; Boettcher, S. W.; Sinton, D.; Sargent, E. H. Bipolar membrane electrolyzers enable high single-pass CO2 electroreduction to multicarbon products. *Nat. Commun.* 2022, *13* (1), No. 3609.

(5) Qiao, J.; Liu, Y.; Hong, F.; Zhang, J. A review of catalysts for the electroreduction of carbon dioxide to produce low-carbon fuels. *Chem. Soc. Rev.* 2014, *43* (2), 631−675.

(6) Kumar, B.; Brian, J. P.; Atla, V.; Kumari, S.; Bertram, K. A.; White, R. T.; Spurgeon, J. M. New trends in the development of heterogeneous catalysts for electrochemical CO2 reduction. *Catal. Today* 2016, *270*, 19−30.

(7) Lu, Q.; Jiao, F. Electrochemical CO2 reduction: Electrocatalyst, reaction mechanism, and process engineering. *Nano Energy* 2016, *29*, 439−456.

(8) Verma, S.; Lu, S.; Kenis, P. J. A. Co-electrolysis of CO2 and glycerol as a pathway to carbon chemicals with improved technoeconomics due to low electricity consumption. *Nat. Energy* 2019, *4* (6), 466−474.

(9) Bajada, M. A.; Roy, S.; Warnan, J.; Abdiaziz, K.; Wagner, A.; Roessler, M. M.; Reisner, E. A Precious-Metal-Free Hybrid Electrolyzer for Alcohol Oxidation Coupled to CO2-to-Syngas Conversion. *Angew. Chem., Int. Ed.* 2020, *59* (36), 15633−15641.
(10) Xie, K.; Ozden, A.; Miao, R. K.; Li, Y.; Sinton, D.; Sargent, E. H. Eliminating the need for anodic gas separation in CO2 electroreduction systems via liquid-to-liquid anodic upgrading. *Nat. Commun.* 2022, *13* (1), No. 3070.
(11) Yue, H.; Zhao, Y.; Ma, X.; Gong, J. Ethylene glycol: properties, synthesis, and applications. *Chem. Soc. Rev.* 2012, *41* (11), 4218−4244.
(12) Hua, X.; Cao, R.; Zhou, X.; Xu, Y. Integrated process for scalable bioproduction of glycolic acid from cell catalysis of ethylene glycol. *Bioresour. Technol.* 2018, *268*, 402−407.
(13) Kahlstorf, T.; Hausmann, J. N.; Sontheimer, T.; Menezes, P. W. Challenges for Hybrid Water Electrolysis to Replace the Oxygen Evolution Reaction on an Industrial Scale. *Global Challenges* 2023, *7* (7), No. 2200242.
(14) Lee, W. H.; Ko, Y.-J.; Kim, J. H.; Choi, C. H.; Chae, K. H.; Kim, H.; Hwang, Y. J.; Min, B. K.; Strasser, P.; Oh, H.-S. High crystallinity design of Ir-based catalysts drives catalytic reversibility for water electrolysis and fuel cells. *Nat. Commun.* 2021, *12* (1), No. 4271.
(15) Reier, T.; Oezaslan, M.; Strasser, P. Electrocatalytic Oxygen Evolution Reaction (OER) on Ru, Ir, and Pt Catalysts: A Comparative Study of Nanoparticles and Bulk Materials. *ACS Catal.* 2012, *2* (8), 1765−1772.
(16) Yao, Y.; Hu, S.; Chen, W.; Huang, Z.-Q.; Wei, W.; Yao, T.; Liu, R.; Zang, K.; Wang, X.; Wu, G.; Yuan, W.; Yuan, T.; Zhu, B.; Liu, W.; Li, Z.; He, D.; Xue, Z.; Wang, Y.; Zheng, X.; Dong, J.; Chang, C.-R.; Chen, Y.; Hong, X.; Luo, J.; Wei, S.; Li, W.-X.; Strasser, P.; Wu, Y.; Li, Y. Engineering the electronic structure of single atom Ru sites via compressive strain boosts acidic water oxidation electrocatalysis. *Nat. Catal.* 2019, *2* (4), 304−313.
(17) Wang, C.; Wu, Y.; Bodach, A.; Krebs, M. L.; Schuhmann, W.; Schuth, F. A Novel Electrode for Value-Generating Anode Reactions in Water Electrolyzers at Industrial Current Densities. *Angew. Chem., Int. Ed.* 2023, *62* (7), No. e202215804.
(18) Yang, Y.; Lie, W. H.; Unocic, R. R.; Yuwono, J. A.; Klingenhof, M.; Merzdorf, T.; Buchheister, P. W.; Kroschel, M.; Walker, A.; Gallington, L. C.; Thomsen, L.; Kumar, P. V.; Strasser, P.; Scott, J. A.; Bedford, N. M. Defect-Promoted Ni-Based Layer Double Hydroxides with Enhanced Deprotonation Capability for Efficient Biomass Electrooxidation. *Adv. Mater.* 2023, *35* (48), No. 2305573.
(19) Wu, H.; Li, J.; Qi, K.; Zhang, Y.; Petit, E.; Wang, W.; Flaud, V.; Onofrio, N.; Rebiere, B.; Huang, L.; Salameh, C.; Lajaunie, L.; Miele, P.; Voiry, D. Improved electrochemical conversion of CO2 to multicarbon products by using molecular doping. *Nat. Commun.* 2021, *12* (1), No. 7210.
(20) An, L.; Chen, R. Recent progress in alkaline direct ethylene glycol fuel cells for sustainable energy production. *J. Power Sources* 2016, *329*, 484−501.
(21) Xin, L.; Zhang, Z.; Qi, J.; Chadderdon, D.; Li, W. Electrocatalytic oxidation of ethylene glycol (EG) on supported Pt and Au catalysts in alkaline media: Reaction pathway investigation in three-electrode cell and fuel cell reactors. *Appl. Catal., B* 2012, *125*, 85−94.
(22) Ravel, B.; Newville, M. ATHENA, ARTEMIS, HEPHAESTUS: data analysis for X-ray absorption spectroscopy using IFEFFIT. *J. Synchrotron Radiat.* 2005, *12* (4), 537−541.
(23) Gann, E.; McNeill, C. R.; Tadich, A.; Cowie, B. C.; Thomsen, L. Quick AS NEXAFS Tool (QANT): a program for NEXAFS loading and analysis developed at the Australian Synchrotron. *J. Synchrotron Radiat.* 2016, *23* (1), 374−380.
(24) Dionigi, F.; Zeng, Z.; Sinev, I.; Merzdorf, T.; Deshpande, S.; Lopez, M. B.; Kunze, S.; Zegkinoglou, I.; Sarodnik, H.; Fan, D.; Bergmann, A.; Drnec, J.; Araujo, J. F. d.; Gliech, M.; Teschner, D.; Zhu, J.; Li, W.-X.; Greeley, J.; Cuenya, B. R.; Strasser, P. In-situ structure and catalytic mechanism of NiFe and CoFe layered double hydroxides during oxygen evolution. *Nat. Commun.* 2020, *11* (1), No. 2522.
(25) Frati, F.; Hunault, M. O. J. Y.; de Groot, F. M. F. Oxygen K-edge X-ray Absorption Spectra. *Chem. Rev.* 2020, *120* (9), 4056−4110.
(26) Drevon, D.; Görlin, M.; Chernev, P.; Xi, L.; Dau, H.; Lange, K. M. Uncovering The Role of Oxygen in Ni-Fe(OxHy) Electrocatalysts using In situ Soft X-ray Absorption Spectroscopy during the Oxygen Evolution Reaction. *Sci. Rep.* 2019, *9* (1), No. 1532.
(27) Jentys, A. Estimation of mean size and shape of small metal particles by EXAFS. *Phys. Chem. Chem. Phys.* 1999, *1* (17), 4059−4063.
(28) Timoshenko, J.; Roese, S.; Hövel, H.; Frenkel, A. I. Silver clusters shape determination from in-situ XANES data. *Radiat. Phys. Chem.* 2020, *175*, No. 108049.
(29) Friebel, D.; Louie, M. W.; Bajdich, M.; Sanwald, K. E.; Cai, Y.; Wise, A. M.; Cheng, M.-J.; Sokaras, D.; Weng, T.-C.; Alonso-Mori, R.; Davis, R. C.; Bargar, J. R.; Nørskov, J. K.; Nilsson, A.; Bell, A. T. Identification of Highly Active Fe Sites in (Ni,Fe)OOH for Electrocatalytic Water Splitting. *J. Am. Chem. Soc.* 2015, *137* (3), 1305−1313.
(30) Görlin, M.; Chernev, P.; Ferreira de Araújo, J.; Reier, T.; Dresp, S.; Paul, B.; Krähnert, R.; Dau, H.; Strasser, P. Oxygen Evolution Reaction Dynamics, Faradaic Charge Efficiency, and the Active Metal Redox States of Ni−Fe Oxide Water Splitting Electrocatalysts. *J. Am. Chem. Soc.* 2016, *138* (17), 5603−5614.
(31) Peng, C.; Ran, N.; Wan, G.; Zhao, W.; Kuang, Z.; Lu, Z.; Sun, C.; Liu, J.; Wang, L.; Chen, H. Engineering Active Fe Sites on Nickel−Iron Layered Double Hydroxide through Component Segregation for Oxygen Evolution Reaction. *ChemSusChem* 2020, *13* (4), 811−818.
(32) Peng, L.; Yang, N.; Yang, Y.; Wang, Q.; Xie, X.; Sun-Waterhouse, D.; Shang, L.; Zhang, T.; Waterhouse, G. I. N. Atomic Cation-Vacancy Engineering of NiFe-Layered Double Hydroxides for Improved Activity and Stability towards the Oxygen Evolution Reaction. *Angew. Chem., Int. Ed.* 2021, *60* (46), 24612−24619.
(33) Wang, B.; Han, X.; Guo, C.; Jing, J.; Yang, C.; Li, Y.; Han, A.; Wang, D.; Liu, J. Structure inheritance strategy from MOF to edge-enriched NiFe-LDH array for enhanced oxygen evolution reaction. *Appl. Catal., B* 2021, *298*, No. 120580.
(34) Wang, M. H.; Lou, Z. X.; Wu, X.; Liu, Y.; Zhao, J. Y.; Sun, K. Z.; Li, W. X.; Chen, J.; Yuan, H. Y.; Zhu, M.; Dai, S.; Liu, P. F.; Yang, H. G. Operando High-Valence Cr-Modified NiFe Hydroxides for Water Oxidation. *Small* 2022, *18* (19), No. 2200303.
(35) Li, Y.; Wu, Y.; Yuan, M.; Hao, H.; Lv, Z.; Xu, L.; Wei, B. Operando spectroscopies unveil interfacial FeOOH induced highly reactive β-Ni(Fe)OOH for efficient oxygen evolution. *Appl. Catal., B* 2022, *318*, No. 121825.
(36) Bai, L.; Lee, S.; Hu, X. Spectroscopic and Electrokinetic Evidence for a Bifunctional Mechanism of the Oxygen Evolution Reaction. *Angew. Chem., Int. Ed.* 2021, *60* (6), 3095−3103.
(37) Lee, S.; Bai, L.; Hu, X. Deciphering Iron-Dependent Activity in Oxygen Evolution Catalyzed by Nickel−Iron Layered Double Hydroxide. *Angew. Chem., Int. Ed.* 2020, *59* (21), 8072−8077.
(38) Xu, Y.; Xia, Z.; Gao, W.; Xiao, H.; Xu, B. Cation effect on the elementary steps of the electrochemical CO reduction reaction on Cu. *Nat. Catal.* 2024, *7* (10), 1120−1129.
(39) Endrődi, B.; Kecsenovity, E.; Samu, A.; Halmágyi, T.; Rojas-Carbonell, S.; Wang, L.; Yan, Y.; Janáky, C. High carbonate ion conductance of a robust PiperION membrane allows industrial current density and conversion in a zero-gap carbon dioxide electrolyzer cell. *Energy Environ. Sci.* 2020, *13* (11), 4098−4105.
(40) Thorson, M. R.; Siil, K. I.; Kenis, P. J. A. Effect of Cations on the Electrochemical Conversion of CO2 to CO. *J. Electrochem. Soc.* 2013, *160* (1), F69.
(41) Frenkel, A. I.; Hills, C. W.; Nuzzo, R. G. A View from the Inside: Complexity in the Atomic Scale Ordering of Supported Metal Nanoparticles. *J. Phys. Chem. B* 2001, *105* (51), 12689−12703.

(42) Zheng, W. iR Compensation for Electrocatalysis Studies: Considerations and Recommendations. *ACS Energy Lett.* 2023, *8* (4), 1952−1958.